Northumbria Research Link

Citation: Sandhu, Jasmine, Rae, Jonathan and Walach, Maria-Theresia (2021) Challenging the Use of Ring Current Indices During Geomagnetic Storms. Journal of Geophysical Research: Space Physics, 126 (2). e2020JA028423. ISSN 2169-9380

Published by: American Geophysical Union

URL: https://doi.org/10.1029/2020JA028423 <https://doi.org/10.1029/2020JA028423>

This version was downloaded from Northumbria Research Link: http://nrl.northumbria.ac.uk/id/eprint/45215/

Northumbria University has developed Northumbria Research Link (NRL) to enable users to access the University's research output. Copyright © and moral rights for items on NRL are retained by the individual author(s) and/or other copyright owners. Single copies of full items can be reproduced, displayed or performed, and given to third parties in any format or medium for personal research or study, educational, or not-for-profit purposes without prior permission or charge, provided the authors, title and full bibliographic details are given, as well as a hyperlink and/or URL to the original metadata page. The content must not be changed in any way. Full items must not be sold commercially in any format or medium without formal permission of the copyright holder. The full policy is available online: http://nrl.northumbria.ac.uk/policies.html

This document may differ from the final, published version of the research and has been made available online in accordance with publisher policies. To read and/or cite from the published version of the research, please visit the publisher's website (a subscription may be required.)

Northumbria University NEWCASTLE

University Library

Check for updates

JGR Space Physics

RESEARCH ARTICLE
10.1029/2020JA028423

Challenging the Use of Ring Current Indices During Geomagnetic Storms

J. K. Sandhu[1], **I. J. Rae**[1], **and M.-T. Walach**[2]

[1]Department of Mathematics, Physics and Electrical Engineering, Northumbria University, Newcastle upon Tyne, UK, [2]Physics Department, Lancaster University, Lancaster, UK

Key Points:

- A superposed epoch analysis is conducted for the ring current spatial distribution during storms
- The DPS relation significantly overestimates ring current energy, particularly at the storm peak
- On average, the ring current energy peaks 6 h later than predicted by the Sym-H index

Supporting Information:

- Supporting Information S1
- Data Set S1

Correspondence to:

J. K. Sandhu,
jasmine.k.sandhu@northumbria.ac.uk

Citation:

Sandhu, J. K., Rae, I. J., & Walach, M.-T. (2021). Challenging the use of ring current indices during geomagnetic storms. *Journal of Geophysical Research: Space Physics*, *126*, e2020JA028423. https://doi.org/10.1029/2020JA028423

Received 3 JUL 2020
Accepted 23 DEC 2020

Abstract The ring current experiences dramatic enhancements during geomagnetic storms; however, understanding the global distribution of ring current energy content is restricted by spacecraft coverage. Many studies use ring current indices as a proxy for energy content, but these indices average over spatial variations and include additional contributions. We have conducted an analysis of Van Allen Probes' data, identifying the spatial distribution and storm-time variations of energy content. Ion observations from the HOPE and RBSPICE instruments were used to estimate energy content in *L*-MLT bins. The results show large enhancements particularly in the premidnight sector during the main phase, alongside reductions in local time asymmetry and intensity during the recovery phase. A comparison with estimated energy content using the Sym-H index was conducted. In agreement with previous results, the Sym-H index significantly overestimates (by up to ~4 times) the energy content, and we attribute the difference to contributions from additional current systems. A new finding is an observed temporal discrepancy, where energy content estimates from the Sym-H index maximize 3–9 h earlier than in-situ observations. Case studies reveal a complex relationship, where variable degrees of agreement between the Sym-H index and in-situ measurements are observed. The results highlight the drawbacks of ring current indices and emphasize the variability of the storm time ring current.

Plain Language Summary The Earth's global magnetic field can trap energetic ions, and during storm times the energy and number of trapped ions increases dramatically. However, the location of the enhancements and how the enhancements vary with time is not fully understood. In this study we have used spacecraft observations to measure changes in the ion population over a large region of space and at different times during storms. The results show that the enhancement is initially very localized, allowing us to identify how the ions are transported to this region. The enhancement then extends to cover a larger region, demonstrating how the ions drift and move spatially. We also compared the results to indirect measurements of the ions' magnetic field perturbation. We find that there are substantial discrepancies between the different measurements, both temporally and in magnitude. The results support previous work that the indirect measurements include significant contamination and do not accurately represent the ring current dynamics during geomagnetic storms.

1. Introduction

Geomagnetic storms were first discovered from observations of large irregular disturbances in the global geomagnetic field (Chapman & Bartels, 1940; Graham, 1724). It was suggested that charged drifting particles in the magnetosphere generate a westward current and an associated magnetic field perturbation that opposes the background geomagnetic field (e.g., Chapman & Dyson, 1918; Chapman & Ferraro, 1930; Singer, 1957). This current is now known as the ring current. The terrestrial ring current is generated predominantly by ~keV ions and is located between ~4 and $7R_E$ (Daglis et al., 1999; Le et al., 2004). During geomagnetic storms, the ring current undergoes significant intensifications, driven by the energization and an increase in the density of the ring current ions (e.g., Gonzalez et al., 1994; Stepanova et al., 2019; Takahashi et al., 1990). The enhanced storm time ring current, and the associated magnetic field perturbations from the westward current, play an important role in a number of magnetospheric processes. These include changes in field line eigenfrequencies that control where ULF wave power can access (e.g., Rae et al., 2019; Sandhu, Yeoman, et al., 2018), as well as providing a source of free energy to drive waves in the inner magnetosphere (e.g., Usanova & Mann, 2016; Yue et al., 2019). Understanding when, where, and how the ring current population is energized is a key motivation.

© 2021. The Authors.
This is an open access article under the terms of the Creative Commons Attribution License, which permits use, distribution and reproduction in any medium, provided the original work is properly cited.

Ground magnetometers whose locations map to the inner magnetosphere can observe north-south magnetic field perturbations induced by the ring current, and fluctuations in this perturbation are often inferred as corresponding to changes in the ring current strength. Ring current indices (such as the Dst index (Sugiura & Poros, 1964), the Sym-H index (Iyemori, 1990), and the SMR index (Newell & Gjerloev, 2012)) are derived from magnetometers that map to this region and cover a range of local times. Furthermore, the magnitude of the indices can be directly related to the total energy content of the ring current population, E_T, using the Dessler-Parker-Sckopke (DPS) equation (Dessler & Parker, 1959; Sckopke, 1966):

$$\Delta B = -\frac{\mu_0}{2\pi}\frac{E_T}{B_0 {R_E}^3}. \quad (1)$$

In Equation 1, μ_0 is the permeability constant ($4\pi \times 10^{-7}$ H m^{-1}), B_0 is the magnetic field strength at the surface of the Earth (3.12×10^{-5} T), and R_E is the radius of Earth ($1R_E$ = 6,372 km). The global magnetic field perturbation, ΔB, can be considered equivalent to the value of a ring current index. Equation 1 provides a relatively simple means to indirectly infer the total energy content of the ring current from the indices and monitor the storm-time variations.

However, Liemohn (2003) reported that the DPS relation makes several key assumptions, such as linear field distortions and a symmetric ring current. In addition, other magnetospheric current systems, notably the tail current and the magnetopause current, can contribute significantly to the observed magnetic field perturbations (e.g., Burton et al., 1975; Turner et al., 2000). Attempts to account for these contributions led to the development of corrected ring current indices, known as the Dst* index and the Sym-H* index (Burton et al., 1975). Furthermore, Gkioulidou et al. (2016) demonstrated that the Sym-H index poorly describes long time scale variations that are driven by the radial diffusion of the high energy ring current ions. Gkioulidou et al. (2016) showed that the high energy ion contribution to the ring current is not well correlated with the absolute value of the Sym-H index and the fluctuations in the Sym-H index are instead dominated by variations in the low energy ion population that occur on much shorter convective time scales.

To assess the accuracy of the ring current indices and the use of the DPS relation, the estimates can be compared to direct in-situ observations of the ring current population. Previous work has shown that in-situ energy density and plasma pressure measurements are typically ~2 times less than the values predicted from the ring current indices (e.g., Ebihara & Ejiri, 2000; Hamilton et al., 1988; Roeder et al., 1996; Turner et al., 2001, 2000; Zhao et al., 2015). However, these studies were often based on single storm events, presenting difficulties in understanding the typical storm-time variations, and made several assumptions regarding energy ranges (neglected low energy populations) and ring current symmetry.

This study aims to identify how the ring current varies temporally during a storm. A statistical analysis of direct in-situ observations was conducted to avoid the assumptions made by the ring current indices and the DPS relation, and also to allow for spatial variations to be explored. The results provide information on where energy is deposited and how ion transport distributes that energy across the inner magnetosphere during storms. We also challenge the use of the ring current indices with the DPS relation by conducting a direct comparison to the in-situ observations.

2. Estimating the Ring Current Energy Content During Storms

2.1. Using Van Allen Probes Data

Direct in-situ observations of the ring current population were obtained from the Van Allen Probes (Mauk et al., 2013), consisting of two identically instrumented spacecraft (Probe A and Probe B). The orbit has a perigee of ~600 km altitude, an apogee of $5.8R_E$ geocentric radial distance, and an inclination of 10°. The orbital period is 9 h and the orbital apogee precesses in local time, such that sampling over all local times is achieved in <2 years. Overall, the Van Allen Probes provide highly suitable coverage of the ring current region, and with data availability from 2012 onwards, the spatial and temporal coverage allows for statistical analysis.

This study employed observations from the Radiation Belt Storm Probes Ion Composition Experiment (RBSPICE) (Mitchell et al., 2013) and the Helium Oxygen Proton Electron (HOPE) (Spence et al., 2013)

instruments. The RBSPICE data sets include: H^+ ions in the energy range of 50–660 keV; O^+ ions in the energy range of 120–990 keV; He^+ ions in the energy range of 60–980 keV. Observations of lower energy ions were provided by the HOPE instrument and these data sets include: H^+ ions in the energy range of 1 eV–50 keV; O^+ ions in the energy range of 1 eV–50 keV. These data sets cover the bulk population of H^+ ions with energies of a few hundred keV (e.g., Krimigis et al., 1985; Sandhu, Rae, et al., 2018). Previous work clearly demonstrates that heavy ions and low energy ions can contribute significantly during geomagnetically active times, and in some cases dominate the ring current population (e.g., Keika et al., 2018; Kistler et al., 2016; Sandhu, Rae, et al., 2018; Stepanova et al., 2019; Zhao et al., 2015). Therefore, the contribution of these ions was also covered in the data sets used.

The data sets provided observations of the omnidirectional ion energy flux and we employed the method of Sandhu, Rae, et al. (2018) and Sandhu et al. (2019) to estimate the energy content in L-MLT bins. The L-MLT coordinate system uses the L value (radial distance of where the given field line crosses the equatorial plane in Earth Radii) as a radial coordinate and the Magnetic Local Time (MLT) value as the azimuthal coordinate. We refer the reader to Sandhu, Rae, et al. (2018) for full details of the methodology and briefly summarize here. The following steps were taken:

1. For each data set, the mean partial ion energy density was estimated from the omnidirectional energy flux, for a spacecraft pass through an L-MLT bin of width ΔL and ΔMLT. The time taken for the spacecraft to traverse the L-MLT is recorded as the uncertainty in the time of measurement (typically 6 min for $\Delta L = 0.5$). The partial ion energy density from each data set (corresponding to a given ion species and energy range) was summed to estimate the total ring current energy density.
2. The volume of the L-MLT bin was then estimated using a dipole magnetic field model scaled for the local magnetic field strength as observed by the Electric and Magnetic Field Instrument Suite and Integrated Science instrument (Kletzing et al., 2013) onboard the Van Allen Probes.
3. The ion energy density was integrated over the volume of the bin to obtain an estimate of the total energy content for the L-MLT bin, E.

This method was applied to all Van Allen Probe A and B data between October 2012 to June 2019 to provide a data set of E values.

It is noted that this approach uses coincident observations from two separate instruments (HOPE and RBSPICE). Significant efforts by the HOPE instrument team have minimized any intercalibration issues in the latest data release (Release 04), such the 87% of ion fluxes agree to within a factor of 2 (see https://www.rbsp-ect.lanl.gov/rbsp_ect.php).

2.2. Using Ring Current Indices

Although there are a range of ring current indices available, the most common being the Dst index, the Sym-H index, and the SMR index, we opted to present a detailed comparison for the Sym-H index. All are derived using a similar method, but key differences relate to the subtraction of baselines, the number of stations used in the calculation, and the cadences of the indices. Our findings are consistent across all indices.

A detailed description of how the Sym-H index is derived is provided by Iyemori (1990) and briefly summarized here. The Sym-H index is calculated with a 1 min temporal resolution from a range of ground magnetometers spanning magnetic latitudes from −47° to 50°. The data are processed in units of one month, and for each month only six stations that are approximately evenly spaced in longitude are used. First, the disturbance component of the measured H (north-south) component is obtained by subtracting the background geomagnetic field and the solar quiet daily variation. Next, a coordinate transformation to the dipole coordinate system is applied. Finally, for each minute, the disturbance component over the six stations is averaged to provide the Sym-H index.

As mentioned previously, attempts to remove contributions from other current systems to the observed Sym-H index have been made, resulting in the corrected Sym-H index. This is termed as Sym-H*. Although there are many different versions of Sym-H*, they generally follow the formulation of Burton et al. (1975):

$$\text{Sym - H}^* = \text{Sym - H} - bP_{\text{dyn}}^{1/2} + c \tag{2}$$

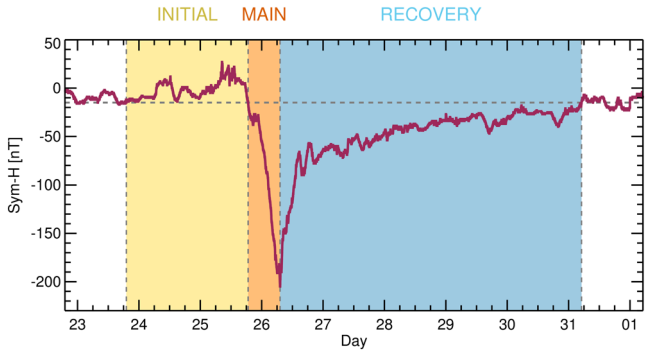

Figure 1. The Sym-H trace during a geomagnetic storm, where the storm peak occurs at 07:11 UT on August 26, 2018. The colored regions show the phase identification using the Walach and Grocott (2019) algorithm, where the initial phase is in yellow, the main phase in orange, and the recovery phase in blue.

where the parameters b and c are empirically determined and P_{dyn} is the solar wind dynamic pressure. In this study, we use the values of b and c determined by O'Brien and McPherron (2000): $b = 7.26$ nT nPa$^{1/2}$ and $c = 11$ nT. The Sym-H* index endeavors to correct for the contribution of magnetopause currents and the quiet day currents.

The calculation of the Sym-H index relies on using observations from magnetometer stations mapping to different MLT sectors of the ring current population and taking an average of those measurements. Therefore, this average perturbation can be considered as describing the symmetric component of the ring current. Alternatively, the Asy-H index can be used to describe the asymmetric component of the ring current (Iyemori et al., 1992). The Asy-H index is derived similarly to the Sym-H index but, instead of averaging the perturbations, the difference between the smallest perturbation and the largest perturbation over the six stations is taken for each minute sample.

For each sample of the energy content provided by the Van Allen Probes, we also took the Sym-H, Sym-H*, and Asy-H indices at the given time. From the data set of Sym-H and Sym-H* values, we estimated the corresponding total ring current energy content for each sample according to the DPS relation (Equation 1).

2.3. Storm Identification

To extract storm time periods for analysis, storms were identified using the algorithm described by Walach and Grocott (2019). The reader is referred to Walach and Grocott (2019) for full details, and we summarize the key aspects here. The algorithm identifies storms from variations in the Sym-H index, and a typical Sym-H index trace is shown in Figure 1. Figure 1 demonstrates the typical features of a geomagnetic storm, which can generally be split into three distinct phases: the initial phase, the main phase, and the recovery phase. The initial phase is present for most storms and is characterized by an enhancement in the Sym-H index driven by enhancements in the magnetopause currents. The initial phase typically lasts ~20 h (Walach & Grocott, 2019). The main phase is identified from a sharp and rapid negative excursion in the Sym-H index, driven by significant energization of the ring current, and has a typical duration of ~8 h (Walach & Grocott, 2019). Finally, the recovery phase, where the Sym-H index gradually increases to quiet time values as the ring current decays, generally lasts several days (Walach & Grocott, 2019). Geomagnetic storms typically exhibit important structure within the recovery phase, namely a two-step decay. In the early recovery phase, the decay of the ring current and consequent increase of the Sym-H index is rapid. This is followed by a lower rate of change in the late recovery phase. The two-step characteristic of the ring current recovery indicates that there are multiple process in operation that occur on different time scales (e.g., Daglis et al., 2003; Hamilton et al., 1988; Jorgensen et al., 2001; Kozyra & Liemohn, 2003).

As well as identifying the storm time periods, the algorithm of Walach and Grocott (2019) also determines the timings of each storm phase. First, a storm is identified as a period where the Sym-H index crosses below a storm time threshold of −80 nT. The storm peak, or alternatively the start of the recovery phase, is marked as the point where the Sym-H index is at its lowest level. The start of the main phase and the end of the recovery phase are then marked as the times immediately prior to and after the storm peak where the Sym-H index is at the quiet time level (here defined as −15 nT). To bound the initial phase, we identify where the Sym-H index reaches a maximum value and then record the time immediately prior to this that the Sym-H index is at the quiet time level. The quiet time threshold of −15 nT and the storm time threshold of −80 nT are taken from Hutchinson et al. (2011).

We note that the Walach and Grocott (2019) algorithm does not distinguish between the early and late recovery phase for storms with a two-step recovery phase, and hence the substructure of ring current variations within the recovery phase will not be the focus of this study. It is hoped that further developments

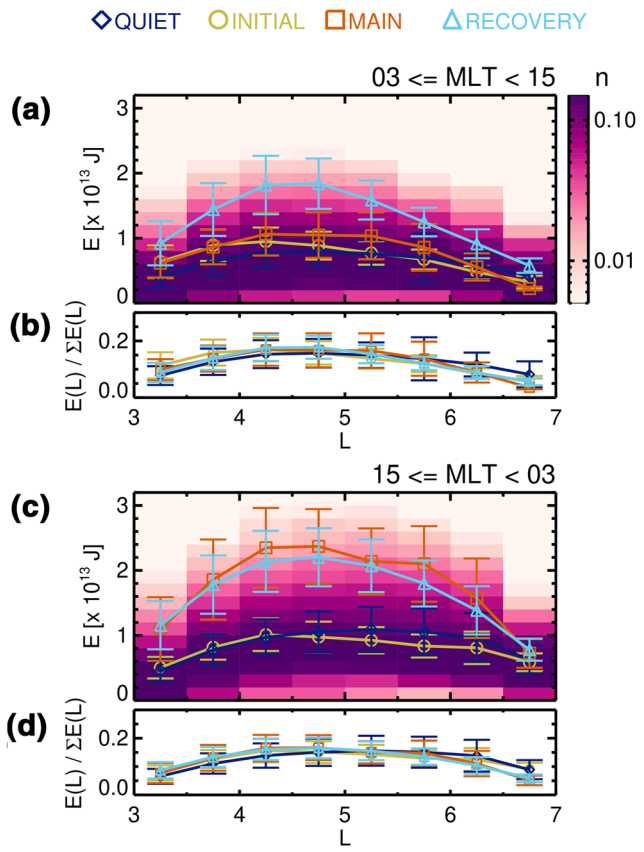

Figure 2. (a and c) The column-normalized number of energy samples binned for L and energy, E (J). The mean energy as a function of L, $E(L)$ is overplotted for quiet times (blue diamonds), storm initial phase (yellow circles), storm main phase (orange squares), and storm recovery phase (blue triangles). The bars indicate the standard deviation of values in the L bin. Panel (a) corresponds to data in the 03 ≥ MLT < 15 sector, and panel (c) corresponds to data in the 15 ≥ MLT < 03 sector. (b and d) The mean energy profiles shown in (a), (c) normalized to the summed profiles, $\Sigma E(L)$ (J). MLT, Magnetic Local Time.

of the algorithm will allow for a detailed analysis of the recovery phase dynamics in a future study.

The Walach and Grocott (2019) algorithm identified 52 storms occurring between 2012 and 2019, and the storm list is included in the Supplementary Information (Data Set S1). Using the storm times, we binned the in-situ measurements, the Sym-H index, and the Sym-H* index for storm phase. The following sections explore how the measurements vary during storm times.

3. Results

3.1. Variations with Storm Phase

Figures 2a and 2c shows the in-situ energy content estimates, E, using a L binsize of 0.5 and an MLT binsize of 3 h, binned for L and E. The color of each bin shows the column-normalized number of samples, considering the full data set. Unlike the Sym-H index, the use of in-situ observations allows for the spatial variations to be explored, and in Figures 2a and 2c we focus on the radial distribution of energy content in the ring current. To account for any local time asymmetries in the ring current energy content we have further binned data for MLT. Figure 2a shows observations in a 12 h bin centered on the prenoon sector (03 ≥ MLT < 15) and Figure 2c is a 12 h bin centered on the premidnight sector (15 ≥ MLT < 03). Previous studies have established that the ring current can exhibit strong local time asymmetries with energy content peaking in the premidnight sector (e.g., Jordanova et al., 2003), and the MLT bins employed in Figure 2 were chosen to center on the regions of maximum asymmetry.

Figures 2a and 2c show that the values typically maximize around $L \sim 5$, and that there is a large variability in values in this region. In the prenoon sector (Figure 2a) the distribution of samples is slightly skewed toward lower L values. In contrast, the premidnight sector (Figure 2c) shows that the distribution is slightly skewed toward higher L values.

Figures 2a and 2c also includes the mean energy profiles, $E(L)$, for the storm initial phases (yellow circles), main phases (orange squares), and recovery phases (light blue triangles). Nonstorm times are labeled as quiet and the mean energy profile is shown by the blue diamonds. The bars on each profile indicate the standard deviations. The profiles show that the energy values during quiet times and the initial phase are similar (~0.8×10^{13} J at $L = 5$). The energy values in the premidnight sector are ~0.1×10^{13} J larger during quiet times compared to during the initial phase, which is attributed to the quiet time intervals containing periods of nonstorm time activity associated with substorm-related enhancements (Sandhu, Rae, et al., 2018; Sandhu et al., 2019) or residual poststorm enhancements of the ring current for example. Furthermore, during the initial phase the increase in solar wind coupling increases the number of ions on open drift paths through an increase in the convection electric field and the earthward displacement of the magnetopause (Ozeke & Mann, 2001; Staples et al., 2020). These ions are then lost through the dayside magnetopause and the average ring current energy content experiences a decrease compared to the quiet time level.

During the main phase, Figures 2a and 2c demonstrate the substantial increases relative to the main phase are observed in the premidnight sector, with values exceeding 2×10^{13} J at $4 \geq L < 5$. In contrast, in the prenoon sector the main phase values are only slightly elevated by ~0.1×10^{13} J compared to the initial phase profile. During the recovery phase, the values remain elevated in the premidnight sector and the profile is very close to the main phase profile (Figure 2c). In the prenoon sector, the values increase substantially compared to the main phase and peaks at ~1.8×10^{13} J. Overall, Figures 2a and 2c shows that large storm

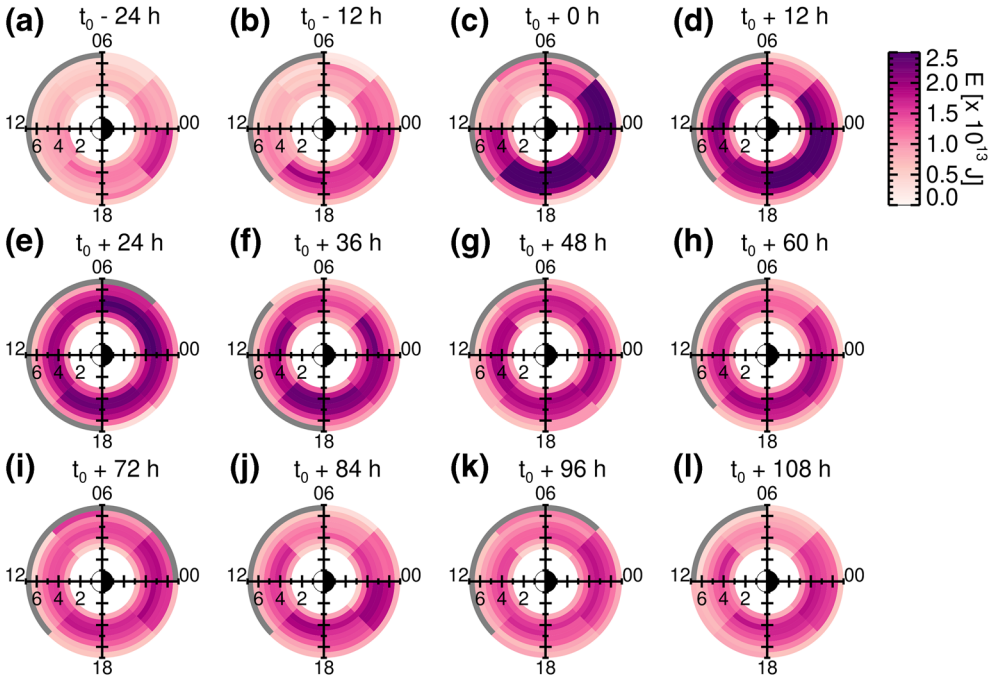

Figure 3. Each panel shows the mean energy, E (J), in L-MLT space. If no samples are present in an L-MLT bin, then the bin is colored gray. Each panel shows samples in a time bin of width 12 h and centered on the time shown. The time bins are relative to the storm peaks (minima in the Sym-H index). MLT, Magnetic Local Time.

time enhancements occur during both the main and recovery phase for the premidnight sector, but are only observed in the prenoon sector during the recovery phase. Furthermore, the magnitude of the enhancement is smaller in the prenoon sector compared to the postmidnight sector.

To examine how the energy is proportioned across L values, Figures 2b and 2d show the relative energy as a function of L. For each profile shown in Figures 2a and 2c, the average energy value in each L bin, $E(L)$, was divided by the sum of the averages over all L bins ($\Sigma E(L)$). Therefore, each bin in Figures 2b and 2d shows the fraction of energy compared to the total ring current energy in the given MLT sector. A comparison of the profiles shown in Figures 2b and 2d demonstrates that the variation with L is very similar for the different geomagnetic conditions, with a very broad peak centered at $L \sim 5$ and large variability across the profile.

However, based on the Sym-H trace the ring current undergoes dramatic changes throughout each storm phase, which cannot be assessed by averaging over each phase. Instead, a superposed epoch analysis was used to explore the variations in energy content during a storm and variations within a storm phase. Figure 3 shows the in-situ energy values (calculated using a L binsize of 0.5 and an MLT binsize of 3 h), where each panel corresponds to a different time relative to the time of the storm peak, where Sym-H is at a minimum ($t = t_0$). Each panel shows the energy values within a time bin of width 12 h and centered on the corresponding time labeled. The data are then further binned for L and MLT, where the mean energy value in each spatial bin is indicated by the color. If there are no samples in a bin then the bin is colored gray. For reference, the number of samples and standard deviations of samples in each L-MLT bin shown in Figure 3 is included in the Supplementary Information (Figures S1 and S2). In general, each bin contains ~10–100 samples. Overall, Figure 3 demonstrates average ring current energy variations during a storm, considering changes in the spatial distribution as well as the magnitude. It is noted that the storm main phases were normalized to a length of 12 h (the mean duration of main phases across the storm studied here), which avoided averaging initial and main phases together and accounted for the large variation in main phase durations.

Figures 3a–3c encapsulate both the initial phase and the main phase, describing variations leading up to the storm peak. We observe that the energy values increase with time. The largest enhancements are observed in the premidnight sector where energy values increase from $\sim 1 \times 10^{13}$ to $\sim 2.5 \times 10^{13}$ J, representing

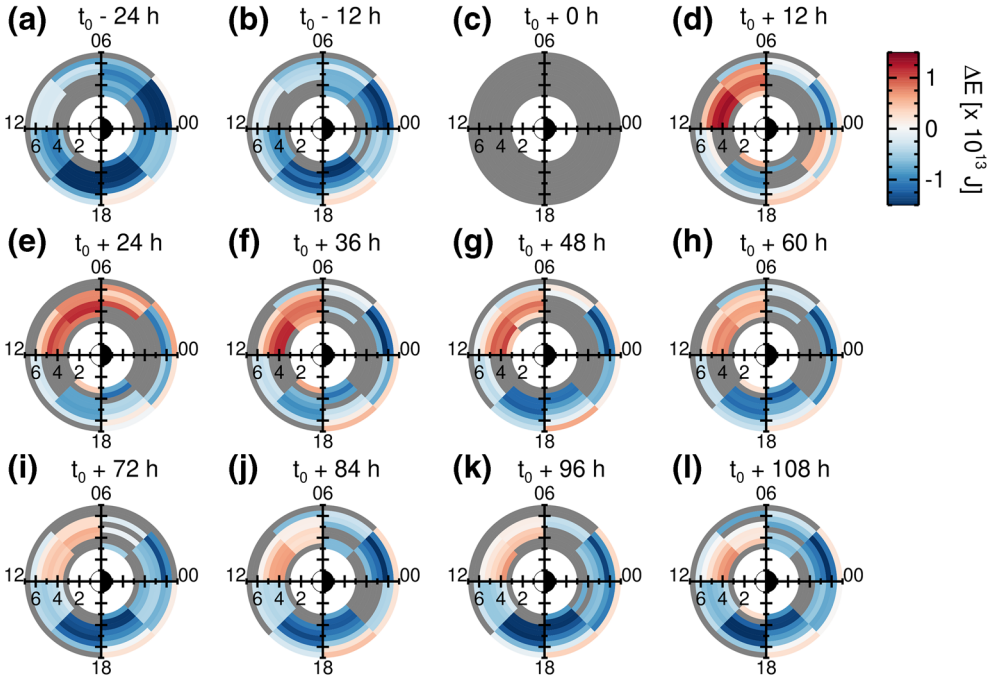

Figure 4. In the same format at Figure 3. The color shows the difference in mean energy compared to the mean energy at $t = t_0$ (Figure 4c) for the same L-MLT bin. The bin is colored gray if the change in energy distributions is not statistically significant according to the Kolmogorov-Smirnov test. MLT, Magnetic Local Time.

an increase of ~150%. The energy distribution at the storm peak (Figure 3c) is highly asymmetric with energy values peaking in the premidnight sector. Following the storm peak, the start of the recovery phase shows that the ring current remains at an elevated state (Figure 3d). However, the energy values are high ($\sim 2 \times 10^{13}$ J) across all MLT sectors and the energy distribution is more symmetric. Throughout the rest of the recovery phase (Figures 3e–3l) the energy distribution remains very symmetric and the magnitude of the energy content values gradually reduce with time.

In order to further analyze temporal variations, Figure 4 shows the energy values relative to the values at the storm peak. Using the same format as Figure 3, each L-MLT bin shows the difference in energy ΔE (J), comparing the mean energy value at that time to the mean energy value at the storm peak in the same spatial bin. In addition, the distribution of energy values is compared using the Kolmogorov-Smirnov test, which allows for an identification of whether the energy distributions have changed significantly. Using a p value threshold of 0.01, distributions that are not significantly different have the corresponding L-MLT bin plotted as gray. If the distributions are different, the ΔE value is plotted, where red corresponds to an increase in energy and blue corresponds to a decrease in energy relative to $t = t_0$. Note that the L-MLT map shown in Figure 4c shows no changes in energy because the values are being compared are identical.

Figures 4a and 4b clearly show that the energy values are lower prior to the storm peak, and that the largest differences are mostly observed in the dusk MLT sector. An interesting feature arises in Figure 4d. The majority of the L-MLT bins show an increase in energy relative to the storm peak. The increases are generally localized to $21 \leq \text{MLT} \leq 00$ and the morning sector with ΔE exceeding $\sim 1 \times 10^{13}$ J. The morning sector enhancement is sustained throughout the recovery phase (Figures 4d–4l), although the magnitude and spatial extent reduces. Elsewhere, the bins show a decrease in energy content with time throughout the recovery phase.

Figures 3 and 4 show interesting local time dependent variations occurring close to the storm peak and in the early recovery phase. To attempt to extract further temporal information, Figure 5 shows the data in the same L-MLT format plots, but using a smaller time binsize of 6 h and focusing on the period from 9 h prior to the storm peak to 15 h after the storm peak. Following the same formats and color scale as Figures 3 and 4, Figures 5a–5d show the mean energy values and Figures 5e–5h show the difference in mean

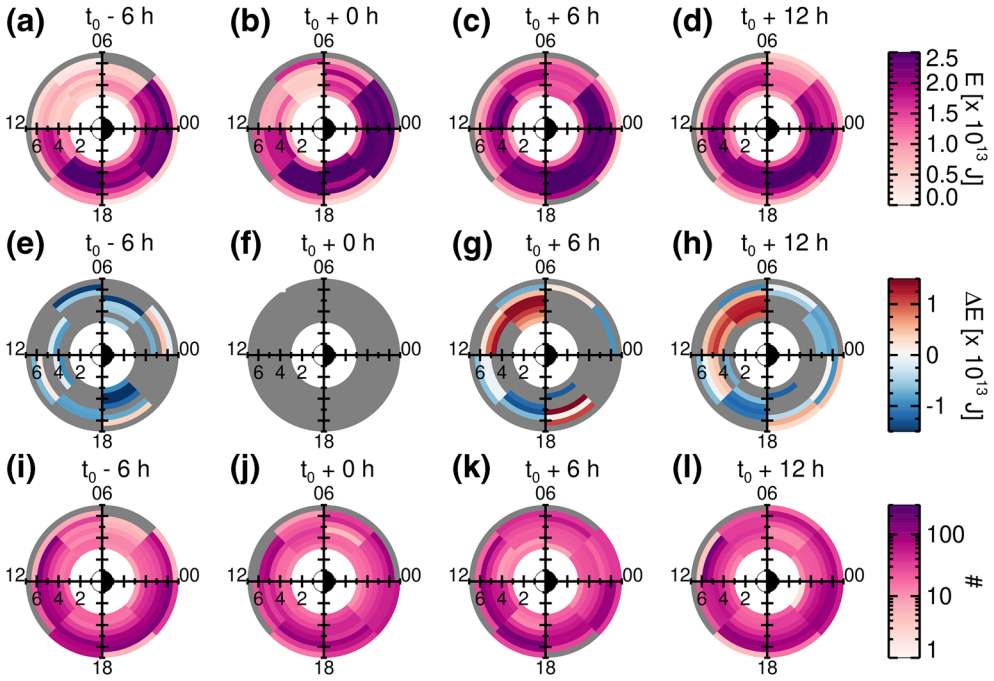

Figure 5. In the same format at Figure 3, but with time bin widths of 6 h (a–d) The color shows the mean energy and a bin is colored gray if no samples are present. (e–h) The color shows the difference in mean energy compared to the mean energy at $t = t_0$ (Figure 4c) for the same L-MLT bin. The bin is colored gray if the change in energy distributions is not statistically significant according to the Kolmogorov-Smirnov test. (i–l) The color shows the number of samples and a bin is colored gray if no samples are present. MLT, Magnetic Local Time.

energy relative to the storm peak. Figures 5i–5l shows the corresponding number of samples in each bin indicating that, although the time bins have decreased in width, sufficient sampling persists across most L-MLT bins. Overall, Figure 5 shows similar features as previously highlighted. The energy values increase from the main phase to the storm peak, resulting in a highly asymmetric ring current, where values peak in the premidnight sector. Following the storm peak, the energy values remain sustained at high levels in the premidnight sector. The ring current also becomes comparatively more symmetric with values increasing in the prenoon MLT sector.

3.2. Comparison to Ring Current Indices

Figures 3–5 demonstrate significant changes in energy content during storms. These results are now compared to the energy content predicted by the Sym-H and Sym-H* indices using the DPS relation.

For context, Figure 6a shows the Sym-H traces of all storms included in the analysis in gray. The mean Sym-H profile as a function of time is shown in blue. Vertical bars indicate the size of the standard deviation. Figure 6a provides insight into the variability across the storms in the range of Sym-H index values.

For a given L-MLT map shown in Figure 5, the mean energy values displayed were summed together to estimate the total ring current energy content, E_T, for the time bin. The time range was also extended from Figure 5 to cover the full storm period. The pink circles in Figure 6b show the total energy, E_T, for each 6 h time bin, plotted relative to the storm peak (noting that the energy axis is reversed here). Using error propagation of the standard deviation values for each L-MLT bin, vertical bars are also included to show the extent of the standard deviation for each time bin. However, due to the standard deviation being relatively small compared to the mean ($\sim 10^{13}$ and <7% of the mean value), they cannot easily be seen in Figure 6b. Horizontal bars show the uncertainty in the mean time for each bin, using the same error propagation techniques. The extent of the bars is again visually small in Figure 6b, with a typical value of 1.6 h. For each time bin, the mean value of the Sym-H and Sym-H* indices is also shown by the blue solid profile and the light blue dashed profile, respectively. The standard deviations are indicated by the extent of the vertical bars,

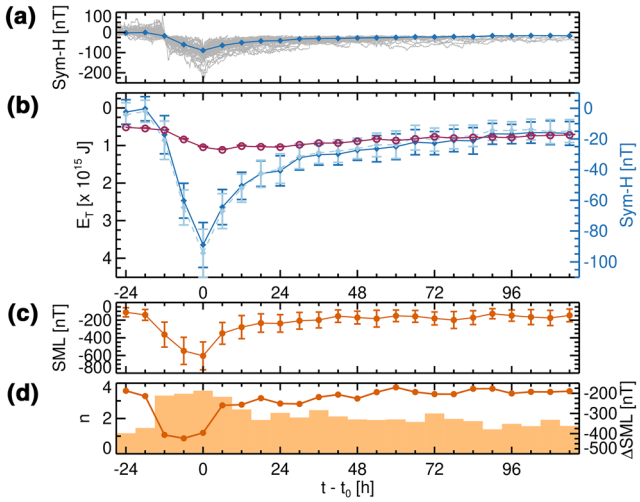

Figure 6. (a) The Sym-H index traces for all storms included in the analysis are shown in gray. The mean and standard deviation of the Sym-H index values are shown by the blue points and bars, respectively. (b) The total ring current energy content, E_T (J), estimated from in-situ observations (pink open circles), the Sym-H index (blue solid), and the Sym-H* index (light blue dashed) plotted as a function of time relative to the storm peak ($t - t_0$). The Sym-H and Sym-H* values (nT) correspond to the right axis, and this axis was aligned with the E_T axis according to the DPS relation (Equation 1). The standard deviations are indicated by the vertical bars and uncertainties in time for E_T are indicated by the horizontal bars. (c) The average SML index (nT) as a function of time relative to the storm peak. The bars indicate the standard deviation in the SML index and the temporal uncertainty. (d) The filled bars show the average number of substorms for each time bin. The circles show the average change in SML index, ΔSML (nT), over substorm expansion phases. DPS, Dessler-Parker-Sckopke.

and the corresponding axis is displayed on the right of the panel. The DPS equation (Equation 1) allows for a direct linear relation of E_T and the ring current indices and was used to align the E_T and the Sym-H index axes shown in Figure 6b. The energy content estimated from the Sym-H and Sym-H* indices under the DPS relation are now directly compared to the in-situ energy values (pink circles).

Figure 6b shows that the in-situ measurements of E_T vary from $\sim 0.4 \times 10^{15}$ to $\sim 1.0 \times 10^{15}$ J, maximizing between 3 and 9 h following the storm peak on a statistical basis. In contrast, the DPS-derived energy content values from the Sym-H index vary from $\sim 0.2 \times 10^{15}$ up to $\sim 3.3 \times 10^{15}$ J at the storm peak. The peak in energy occurs at $t = t_0$ by definition of the storm peak. It is also noted that the peak is substantially more defined than the peak in the in-situ energy values. Figure 6b shows that the range in these energy values (see blue bars) is largest at the storm peak, suggesting a large variability in the energy content at this time across different storms. The energy content values predicted from the corrected ring current index, Sym-H*, show a largely similar temporal dependence to the values using Sym-H. The magnitudes using Sym-H are also very similar to Sym-H*, differing by $< \sim 0.1 \times 10^{15}$ J.

Although the peak in E_T appears comparatively slight, partly due to the large y axis range, we emphasize that the result is underpinned by statistical testing (see Figure 4). Furthermore, comparisons of sample distributions for adjacent temporal bins around the E_T peak show significant differences according to the Kolmogorov-Smirnov test with a confidence level of >99.99% (not shown for brevity).

It is noted here that the time binsize of 6 h is chosen, although we find that the minimum in observed E_T remains at $t = t_0 + 6$ h when smaller time binsizes are used (not shown). However, binsizes smaller than 6 h have significantly reduced statistical significance. Furthermore, for binsizes smaller than the duration of a full spacecraft pass through the ring current region (4.5 h) leads to inconsistent spatial sampling between time bins.

Previous work has identified that the tail current systems can contribute significantly to the observed ring current indices during substorms (e.g., Belova & Maltskv, 1994; Kalegaev et al., 2005; Ohtani et al., 2001; Siscoe & Petschek, 1997; Turner et al., 2000). Turner et al. (2000) shows that the tail current contributes ~25% to the observed ring current index value during both storm time and nonstorm time substorms. To identify whether there was substorm activity during the storms analyzed here, and hence important tail contributions to the Sym-H and Sym-H* indices, we include the average SML index trace in Figure 6c. The SML index can be considered as equivalent to the AL index in terms of construction, and describes the strength of the high latitude nightside westward auroral electrojets (Gjerloev, 2012; Newell & Gjerloev, 2011). In contrast to the AL index, the coverage of ground magnetometers used for the SML index extends over a larger range of latitudes (40–80° magnetic latitude) and will provide reliable measurements of the storm time westward auroral electrojet (Ahn et al., 2005; Feldstein et al., 1999). Reductions in the SML index are signatures of substorm activity and the magnitude of the reduction over the substorm expansion phase is an indicator of the substorm size. Figure 6c shows a decrease in the SML index during the storm, centered around the storm peak ($t = t_0$).

In order to investigate the role of substorm activity, the SOPHIE (Substorm Onsets and Phases from Indices of the Electrojet) identification technique is employed to identify the occurrence and properties of substorms during each storm (Forsyth et al., 2015). In this study, the SOPHIE technique identifies substorm expansion phases based on percentiles of the rate of change of the SML index (using an expansion percentile threshold of 75), where SML is the lower component of the SuperMAG auroral electrojet index. During

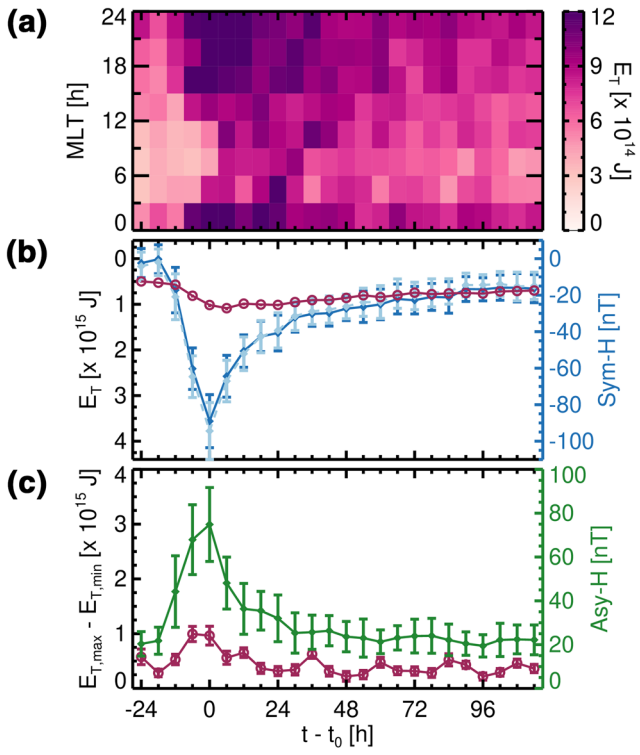

Figure 7. (a) Total ring current energy content, E_T (J) binned for MLT (h) and time relative to the storm peak, $t - t_0$ (h). (b) The average ring current energy content, E_T (J), estimated from values shown in Figure 7a (pink open circles), the Sym-H index (blue solid), and the Sym-H* index (light blue dashed) plotted as a function of time relative to the storm peak ($t - t_0$). The Sym-H and Sym-H* values (nT) correspond to the right axis, and this axis was aligned with the E_T axis according to the DPS relation (Equation 1). (c) The difference between the maximum and minimum values shown in Figure 7a (pink open circles) and the Asy-H index (green solid) plotted as a function of time relative to the storm peak ($t - t_0$). The Asy-H values (nT) correspond to the right axis, and the axis was aligned with the left axis according to the DPS relation (Equation 1). The standard deviations are indicated by the vertical bars and the uncertainty in time is indicated by the horizontal bars for the pink profiles. MLT, Magnetic Local Time; DPS, Dessler-Parker-Sckopke.

enhanced magnetospheric convection the SML index will exhibit substorm-like reductions and these fluctuations are also reflected in the SMU index (the upper component of the SuperMAG auroral electrojet index), whereas during substorms the SML and SMU index vary relatively independently (Rostoker, 1972). In order to identify whether an expansion phase identification corresponds to a period of enhanced convection (a false identification), the SOPHIE technique also consults variations in the SMU index and removes identifications where the SML and SMU indices are varying in a similar way. For full details on the SOPHIE technique, the reader is referred to Forsyth et al. (2015). Using the SOPHIE identifications, Figure 6d shows the average number of substorms in a given time bin, indicated by the height of the filled bars. The number of substorms maximize at the storm peak with an average of 3–4 substorms occurring for a typical storm. The circles in Figure 6d show the average size of the substorm, where the size was inferred from the change in the SML index over the substorm expansion phase. We also identify that substorms are, on average, largest at the storm peak.

Although the energy content of the ring current is estimated by summing over all local time sectors and accounts for any local time dependences in energy content, the Sym-H index is constructed by averaging over local time asymmetries. In order to more accurately compare the E values observed with the Sym-H indices, an alternative approach can be adopted that aims to replicate the Sym-H generation technique. At a given time and for a given MLT sector shown in Figures 5a–5d, the values were summed over L bins to provide the energy content for the MLT sector. The value was then integrated to cover 24 h of MLT, and from a single MLT sector estimate the total ring current energy content, E_T. This echoes the Sym-H technique, where each magnetometer measures perturbations that would correspond to a hypothetical symmetric ring current across all MLTs. The construction of the Sym-H index then averages the measurements from six magnetometer stations to describe the average ring current over all local times. Essentially, the resultant E_T values can be interpreted as what a single magnetometer would measure as the total ring current energy. Figure 7a shows the E_T values binned for MLT and time relative to the storm peak. The color of the bin shows the E_T value. Figure 7a demonstrates the key storm time features that have been previously identified. Specifically, we observe increases in energy content during the main phase that maximize close to the storm peak and gradually decay throughout the recovery phase. The ring current is also highly asymmetric around the storm peak, with values maximizing in the premidnight MLT sector, and increasingly symmetric following the storm peak.

The Sym-H index is generated by averaging perturbations from a range of local times. Figure 7b shows the result of averaging values shown in Figure 7a across all MLT sectors, considering each time bin separately. The pink open circles show the mean E_T value, and the error-propagated standard deviation is shown by pink bars. (As before the bars are considerably smaller than the range of the axes and are not easily visible). The corresponding mean Sym-H and Sym-H* values as a function of time are shown by the blue solid and light blue dashed profiles, respectively. The bars show the width of the standard deviation. The y axes are scaled according to the DPS relation (similarly to Figure 6b). Overall, the profiles show the same features as discussed from Figure 6b. The estimates of total energy content are extremely similar in both magnitude and temporal variation, and it appears that the alternative technique has little impact on the estimations.

An advantage of the technique is the ability to conduct a comparison to the Asy-H index. As described in Section 2.2, the Sym-H index is the average over the perturbations measured across stations whereas the Asy-H index is the difference between the maximum and minimum perturbations across stations. Figure 7c

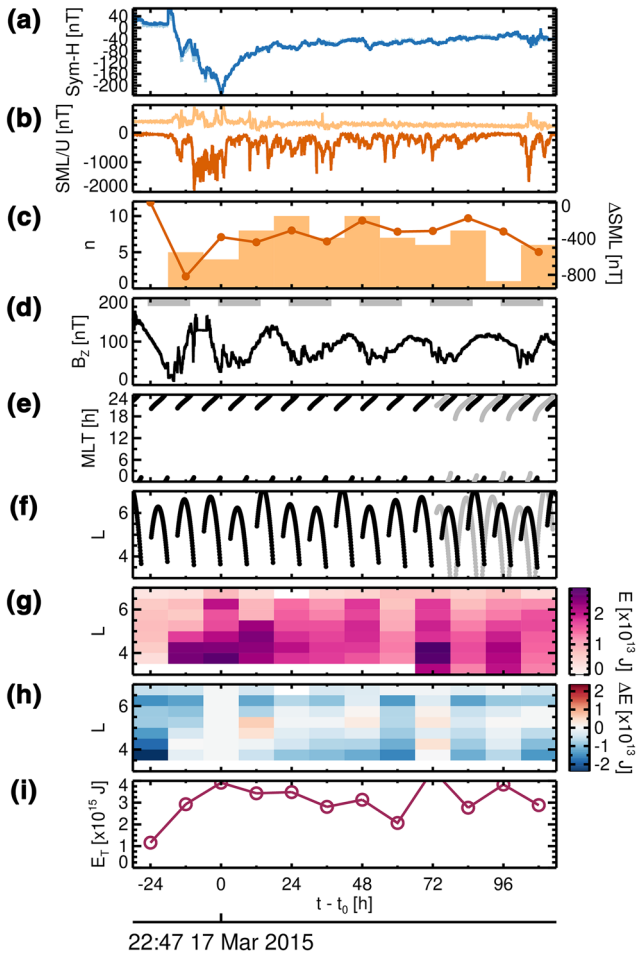

Figure 8. Magnetic indices and in-situ observations of energy content during a storm, where the storm peak occurred at 22:47 UT on March 17, 2015. The values are plotted relative to the time of the storm peak ($t - t_0$). (a) Sym-H (blue) and Sym-H* (light blue) indices (nT). (b) SML (orange) and SMU (light orange) indices (nT). (c) The number of substorms for each time bin (filled bars) and the average change in SML index, ΔSML (nT), over substorm expansion phases (circles). (d) B_z (nT) component of the magnetic field observed by the GOES 15 spacecraft, where the gray bars at the top of the panel indicate when GOES 15 is located in the nightside sector (18 < MLT < 06). The (e) MLT and (f) L value of Van Allen Probe A (black) and B (gray). (g) Energy content, E (J), for L-MLT bins of width $\Delta L = 0.5$ and $\Delta\text{MLT} = 24$ h. (h) Energy content of an L-MLT bin relative to the value of the bin at $t - t_0$. (i) The total energy content, E_T over all spatial bins for each time bin. MLT, Magnetic Local Time.

shows the mean Asy-H index as a function of time in green, where the bars indicate the standard deviation across values. Using the E_T values shown in Figure 7a, the maximum and minimum E_T value across the range of MLT sectors can be taken for each time bin. The pink profile in Figure 7c shows the difference between the maximum and minimum values for each time bin, the vertical bars shows the error-propagated standard deviation, and the horizontal bars show the uncertainty in time. Note that the y axes are scaled according to the DPS relation. Both the energy values and the Asy-H profiles show similar temporal variation. The values increase during the main phase and maximize at the storm peak (within ±3 h). The values then reduce throughout the recovery phase, with a rapid recovery in the early recovery phase and a comparatively gradual recovery in the late recovery phase. The variability in values is largest at the storm peak. These trends arise as the ring current is highly asymmetric at the storm peak and gradually becomes increasingly symmetric during the recovery phase (Figures 3 and 7a). Interestingly, we note that the peaks in observed asymmetry and intensity occur at different times during the storm, on average. Whereas the observed energy content (shaped by the magnitudes of ion source and loss processes) maximizes at $3 \leq t_0 < 9$ h, the asymmetry (dominated by drift path configurations that control the ratio of open and closed drift paths) maximizes at $-3 \leq t_0 < 3$. Figure 7c also shows that there are significant differences in magnitude between the observed energy values and the Asy-H index especially at the storm peak, similarly to the comparison to the Sym-H index. The source of the discrepancy is expected to be the same as the discrepancies with the Sym-H index, and will be discussed in the following section.

3.3. Case Studies

Figures 6b and 7b demonstrate that there is a statistical difference in the temporal profile of the energy content estimated using ring current indices with the DPS relation and of the in-situ estimates, such that the in-situ values peak ~6 h later. Is this a feature consistent across all storms or is it a result of averaging storms with different temporal trends? In order to shed light on this question, we present a selection of case studies, shown in Figures 8 and 9.

As before, the time series are plotted relative to the storm peak, defined using the Sym-H index. The Sym-H (blue) and Sym-H* (light blue) indices (nT) are shown in panel (a) and the SML (orange) and SMU (light orange) indices (nT) are shown in panel (b). The enhanced level of magnetospheric convection during the storm main phase is apparent from the simultaneous increase in the SMU index with the decrease in the SML index. Superimposed deviations in the SML index, with no corresponding changes in the SMU index, are also evident throughout both events and indicate the occurrence of substorms. Panel (c) shows the number of substorms in each time bin (filled bars), as identified using the SOPHIE technique, as well as the average change in SML index over the substorm expansion phases (circles). The B_z (nT) component of the magnetic field, as observed by GOES 15, is shown in panel (d). Periods when GOES 15 is located in the nightside magnetosphere (18 < MLT < 06) are indicated by the gray bars at the top of the panel. Figures 8d and 9d both show rapid (<~1 h) enhancements in the B_z component throughout the storm period, indicative of substorm-associated dipolarizations of the magnetic field.

The Van Allen Probes MLT and L location are shown in panels (e), (f), in black for Probe A and in gray for Probe B. Both case studies have consistent L coverage across the time period of the storm. Figure 8e shows

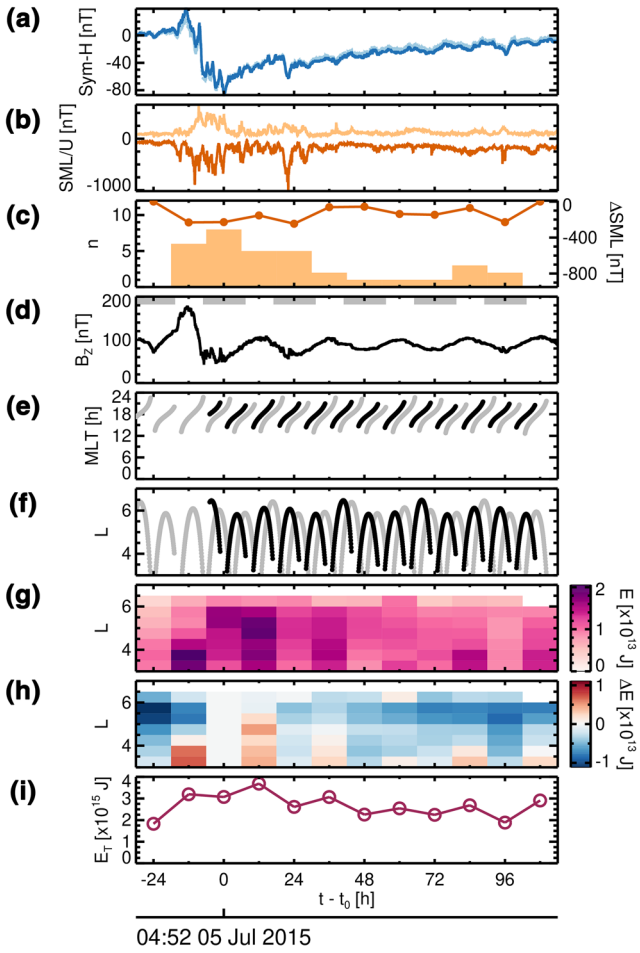

Figure 9. Magnetic indices and in-situ observations of energy content during a storm, where the storm peak occurred at 04:52 UT on July 5, 2015, using the same format as Figure 8.

spacecraft passes through the midnight sector, and Figure 9e shows sampling of the dusk region. Panel (g) shows the L-MLT bins of width $\Delta L = 0.5$ and $\Delta\text{MLT} = 24$ h, where the color of the bin indicates the mean energy content, E (J). Figures 8g and 9g show variations in the energy content during the storm period, with the values increasing across almost all L values then decreasing. However, the duration of the enhancement differs between the case studies. In order to extract changes in energy content relative to the time of the storm peak, panel (h) shows the difference in mean energy content relative to $t = t_0$, ΔE (J), for the same spatial bin. Prior to the storm peak, the energy values are reduced by $\sim 10^{13}$ J. Following the storm peak, Figure 8 shows a general decrease in energy whereas Figure 9 shows initial enhancements in the early recovery phase followed by a decrease after a few days. The variation is further explored in panel (i), which shows the estimated total energy content, E_T (J), obtained by summing over the spatial bins for each time bin. As some time periods have L bins with no sampling, the L dependence shown in Figure 2b is used to extrapolate over the $3 \leq L \leq 7$ region. Figures 8h and 8i show that the energy content increases prior to the storm peak, over the main phase, and then maximizes at the storm peak, following a gradual reduction in the energy content over the recovery phase. This closely follows the temporal trends of the ring current indices. Figures 9h and 9i similarly show that the energy content increases over the main phase. However, following the storm peak ($t > t_0$) there is continued enhancement and the energy content peaks ~12 h afterward. This is in agreement with the statistical trends shown in Figure 4.

It is noted here that larger time bins are used compared to Figure 6. This was to avoid differences between inbound and outbound spacecraft passes (which sample different MLT sectors) being interpreted as temporal variations. Using a time bin of 12 h ensures that a full orbit is sampled.

4. Discussion and Interpretation

The results demonstrate clear and statistically significant changes in the energy content, both in magnitude as well as local time distribution. Prior to the storm peak and during the main phase, the ring current undergoes large global enhancements with the energy content more than doubling in some regions. Interestingly, the L shell dependence is observed to be relatively independent of storm phase, where the L profile shown in Figure 2b is similar for both storm times and quiet times. The peak in energy content does not demonstrate any observable change in L location. Although some previous work suggests that the peak moves Earthwards during storm times (e.g., Hamilton et al., 1988; Roeder et al., 1996), Zhao et al. (2015) observes that the energy density peak does not exhibit substantial changes in L position. Zhao et al. (2015) asserts that although the low energy ion contribution is significant during storm times and moves to lower L values, the higher energy (more than few hundred keV) H^+ contribution that is neglected in some studies does not change significantly in L location. Therefore, the higher energy ions continue to control the location of the ring current energy peak and, especially for small and moderate storms, are critical in determining the L distribution of energy content. The results shown here support the conclusions of Zhao et al. (2015), and suggests that the higher energy ions are dominant in shaping the L profile on a statistical basis.

In terms of the MLT distribution, Figures 5 and 7 demonstrate that during the main phase, the energy content is highly asymmetric and the values peak in the premidnight sector. This feature is well documented and attributed to the enhanced supply of plasma from the nightside plasma sheet via injection and convection (e.g., Antonova & Ganushkina, 1997; Buzulukova et al., 2010; Ebihara & Ejiri, 2000; Ebihara et al., 2002; Fok et al., 1996; Katus et al., 2013; Li et al., 2011; Lui, 2003; Perez et al., 2012). Due to strongly enhanced electric fields in the inner magnetosphere, the ring current is dominated by ions on open drift

paths. Ions enter the inner magnetosphere on the nightside, experience westward drift, and are lost to the duskside magnetopause, thus generating the local time asymmetry (Liemohn et al., 2001, 2015; Milillo et al., 2003; Mouikis et al., 2019; Takahashi et al., 1990).

Closely following the storm peak ($3 \leq t_0 < 9$ h), the ring current becomes more symmetric. Figure 5 shows enhancements on the nightside corresponding to continued and increased transport of plasma from the nightside plasma sheet. Relative enhancements on the dayside arise from a subsidizing of the convection electric field, allowing ions to be trapped on closed drift paths and access all local time sectors (e.g., Daglis et al., 2003; Liemohn et al., 2001). The drift of ions from the duskside on closed drift paths acts to reduce the local time asymmetry (Antonova et al., 2014; Ebihara & Ejiri, 2000). Throughout the recovery phase, the ring current asymmetry continues to decrease as the ions drift and populate all local time sectors (Ebihara & Ejiri, 2000). The energy content gradually reduces due to a multitude of ring current loss process, namely charge exchange (Antonova, 2006; Dessler & Parker, 1959; Hamilton et al., 1988; Welling et al., 2015).

4.1. Discrepancies Between the Ring Current Energy Content and the Ring Current Indices

Although both the in-situ observations and energy values derived using the DPS relation with ring current indices show the same general trends, where the energy content increases during the main phase then gradually reduces in the recovery phase, there are also significant discrepancies in the magnitude and temporal variations. These are clearly apparent from Figure 6a. We find that during the storm period, the in-situ estimates are ∼50% smaller than the estimates using Sym-H and Sym-H*, and are almost 4 times smaller at the storm peak.

The observed discrepancy may initially appear to contradict some previous results. For example, Greenspan and Hamilton (2000) show that, on average, during geomagnetic storms the DPS relation is upheld with no significant discrepancy between the Dst index and in-situ measurements. However, a key factor relating to the Greenspan and Hamilton (2000) study and others is that the statistical analyses consider the full storm interval and instead order observations using ring current indices (whereas in this study we separate samples according to storm phase). Due to the comparatively longer duration of the recovery phase compared to the main phase, the statistical storm time analysis will be mostly represented by recovery phase samples. The results shown here suggest that the statistically significant discrepancy with the DPS relation predominantly occurs in a relatively small period of time compared to the storm length and compared to the recovery phase duration. Therefore, we suggest that time periods where the DPS relation is not a good description is not statistically significant when Greenspan and Hamilton (2000) and others consider the full storm period. On this basis, it is justified that these results do not necessarily contradict previous work, but instead highlights the capabilities of different analysis techniques to understand the temporal evolution during geomagnetic storms. Furthermore, previous studies also report a difference in magnitude between observed ring current energy content and values derived from ring current indices with the DPS relation. For example, Hamilton et al. (1988) observes that ring current energy content ranges from 1 to 4 times smaller than the estimates using the DPS relation applied to the Dst index. Previous work attributes discrepancies in the magnitude to a variety of factors, which will now be discussed in the context of this study.

4.1.1. Unrepresentative in-Situ Estimates

The in-situ estimates of ring current energy content assume that the total energy is contributed by ions within an L range from 3 to 7. If these assumptions disregard a population or region that contributes a substantial amount of energy to the ring current, then the approach will underestimate the total ring current energy content. Although it is assumed that the ring current is carried solely by ions and neglects electron contributions, results from Zhao et al. (2016) show that this is a reasonable premise. Zhao et al. (2016) demonstrated the electrons contribute ∼12% of the energy content for a moderate storm, and even less for intense storms. The electron contribution is clearly insufficient to be dominating the observed discrepancy.

In terms of the L range considered, Zhao et al. (2015) identified that ring current ions at radial distances outside the Van Allen Probe coverage have a very small contribution due to the steep radial gradient in

energy density. Therefore, we conclude that the L range is not excluding a substantial portion of the ring current energy density.

4.1.2. Contributions From Other Current Systems

A breadth of the published literature demonstrates that the Sym-H index includes significant contributions from additional magnetospheric current systems:

1. *Internal magnetic fields*: Dessler and Parker (1959) showed that for a perfectly diamagnetic Earth, the magnetic field perturbation is multiplied by ∼50% at the equator. Langel and Estes (1985) suggested that the observed ring current indices should be multiplied by 0.3–0.5 in order to mitigate for this contribution.
2. *The magnetopause*: Enhancements in the magnetopause current contribute positively to the measured magnetic field perturbation, as demonstrated by strong correlations between the solar wind dynamic pressure and ring current indices (Stepanova et al., 2019). In order to account for this contribution, Burton et al. (1975) suggested the use of a corrected ring current index. However, Figure 6a shows that the discrepancy persists.
3. *The substorm current wedge*: When a substorm current wedge is present, ground magnetometer stations located outside the wedge experience an additional negative perturbation and stations located inside the wedge experience a positive perturbation. If the station coverage is uniform, then this effect is averaged out. If station coverage is limited, then the contribution from the substorm current wedge can be significant, with reports that the perturbation is comparable to the tail current effects (Friedrich et al., 1999; Munsami, 2000). The Sym-H index is derived from only six magnetometer stations, suggesting that the substorm current wedge effects could be important. However, the large similarity in results when the SMR index is used instead (derived from ∼100 stations (Newell & Gjerloev, 2012)), indicates that this is unlikely to be the dominant driver of the discrepancy with in-situ estimates.
4. *The tail current*: As previously mentioned, preceding work shows that the tail current is a significant contributor to the observed ring current indices, representing ∼25% of the measured perturbation (e.g., Turner et al., 2000). Dubyagin et al. (2014) observed a nearly linear relationship between the ring current index and the tail current contribution, and concluded that the tail current is a dominant factor compared to the other additional current systems. Furthermore, Kalegaev et al. (2005) establishes that during moderate storm times, the tail current and ring current contributions to ring current indices are comparable, although the tail current contribution is less important for intense storms.

4.2. The Role of Substorms

Figure 6a shows a temporal discrepancy, where the in-situ energy content estimation peaks, on average, at a later time ($3 \leq t_0 < 9$ h) than estimates using the Sym-H index. From an examination of in-situ tail current observations, Ohtani et al. (2001) found that there is a tendency for a substorm onset to occur at the storm peak. The authors suggest that the associated reduction of the tail current following substorm onset drives a corresponding reduction in the magnitude of the observed Sym-H index (see also Friedrich et al., 1999; Iyemori & Rao, 1996). Therefore, Ohtani et al. (2001) concluded that the start of the recovery phase (or equivalently the time of the storm peak), where the Sym-H index begins to increase, is due to the tail current dynamics and independent of the ring current intensity. Furthermore, Ohtani et al. (2001) suggest that a substorm onset would act to increase the ring current enhancement following the storm peak through substorm-associated ion injections. They also noted that the estimates of the tail current contribution are restricted by spacecraft coverage. The contribution to the Sym-H index is likely to be even larger as they cannot measure how widely and completely the tail current is disrupted. This effect is also supported by modeling results, where Kalegaev et al. (2005) showed that the tail current begins to decay while the ring current continues intensifying during a storm. The substorm-related recovery of the tail current was estimated to cause an increase in the Dst index by ∼50 nT for a moderate storm.

However, the analysis conducted by Ohtani et al. (2001) considered the effect of a single substorm and showed that the storm peak in Sym-H would be shifted by ∼1 h earlier (time scale for a substorm). To support the observations shown in Figure 6a, where the storm peak is shifted by several hours, we require a sustained and continued period of substorm activity. This is confirmed by Figures 6b and 6c. We observe

substorm activity throughout storms, but the frequency and substorm size clearly maximizes at the storm peak. The high level of substorm activity not only reduces the tail current contribution, but also enhances the supply of plasma to the ring current region. Substorms are associated with long lived and substantial enhancements in ring current ion fluxes through enhanced convection and injection events (e.g., Reeves & Henderson, 2001; Sandhu, Rae, et al., 2018; Sandhu et al., 2019; Yue et al., 2018). For example, Gkioulidou et al. (2014) demonstrates that substorms play a crucial role in contributing to and building up ring current energy content during geomagnetic storms. The continued transport of plasma from the nightside plasma sheet is evident from the nightside enhancements following the storm peak (Figure 4d).

Figure 9i provides an example of continued ring current energization following the storm peak. Figure 9b shows both enhanced convection as well as intensified levels of substorm activity throughout the main phase and around the storm peak. The substorm identifications shown in Figure 9c demonstrate that as well as heightened substorm occurrence (eight substorms occurring close to the storm peak), the average size of these substorms is slightly increased with an average $\Delta SML \sim -300$ nT. The magnetic field observations at geosynchronous orbit, provided by the GOES 15 spacecraft and shown in Figure 9c, indicate coincident dipolarization signatures on the nightside and provides support for the enhanced level of substorm activity during the main phase. The frequency and size of substorms then subsides during the recovery phase (Figures 9b–9d).

In contrast, Figure 8i shows that the ring current energy content peak is coincident with the storm peak. For this storm, there is significant substorm activity during the early main phase (five substorms with an average size of ~800 nT) which is reflected in slight positive perturbations in the Sym-H trace (Figures 8a–8d). However, at the storm peak, the level of substorm activity is considerably decreased. Comparing Figure 8c to Figure 9c reveals that the average substorm size is approximately halved. However, during the recovery phase the number of substorms is markedly elevated. High numbers of substorms are observed with coincident dipolarization signatures (Figures 8c and 8d). For this storm, we suggest that the low level of substorm activity during the end of the main phase did not significantly change the tail current. The start of the recovery phase in the Sym-H index is not thought to be driven by tail current dynamics, and instead is driven by the ring current. Although there is observed substorm activity during the recovery phase and the early main phase, the dynamics at the storm peak would be the key factor for causing an early recovery in the Sym-H index and generating a temporal discrepancy between the Sym-H index and the in-situ energy values.

Overall, Figures 8 and 9 show that although the Sym-H trace tends to show similar temporal trends, the ring current energy content variation with time is more variable. This variability in the level of agreement between the in-situ observations and Sym-H trace is further supported by additional case studies (not shown here for brevity). We suggest that the varying timing discrepancy between the storm peak and the maximum in ring current energy content may be dominated by varying levels of substorm activity during a storm. A comparison between Figures 8b and 8c and 9b and 9c shows that the level of substorm activity varies significantly between individual storm events, so the dominance of the tail current dynamics close to the storm peak is expected to also vary substantially between events.

As the energy content maxima occurs at varying times relative to the storm peak, the superposed epoch analysis approach has averaged over peaks occurring at different points. This leads to the very broad peak in energy content shown in Figure 6a. In order to further investigate when the ring current energy content peaks, without applying assumptions of local time asymmetries on a spacecraft sampling a single MLT sector, we require global, multipoint measurements of the inner magnetosphere. Future work will focus on multispacecraft analysis of the ring current during storm times to investigate the temporal profiles further.

5. Conclusions

Spatial variations in energy content during geomagnetic storms were explored using observations from the HOPE and RBSPICE instruments onboard the Van Allen Probes. The presence of an asymmetric ring current, with significant energy enhancements in the premidnight MLT sector, agrees with previous work and provide information on ion trajectories in the inner magnetosphere. The distribution of energy content

with L shows little change with storm phase, supporting previous results that the high energy population dominates the peak location.

A superposed epoch analysis revealed important discrepancies between in-situ energy content measurements and estimated values using ring current indices. In agreement with previous results, the Sym-H index combined with the DPS relation severely overestimates the ring current energy content. Statistically, there are substantial temporal discrepancies, such that energies estimated using the Sym-H index peak at an earlier time than the ring current energy content. The magnitude of this discrepancy is on average between 3 and 9 h, and a suggested cause is intense substorm activity occurring at the end of the main phase. The discrepancies in magnitude and timing persist for the Sym-H* index, the Dst index, the SMR index, and the partial SMR indices. An analysis of case studies shows that level of agreement between the ring current indices and the ring current energy content is highly variable. We emphasize that the substorm-ring current relationship is complicated. Although previous studies (e.g., Ohtani et al., 2001) provides some basis for the proposed mechanisms, further quantitative analysis of the tail current contribution to the Sym-H index is essential for validating the suggested role of substorm activity.

Overall, this work highlights the level of variability across storms, and proposes the importance of substorms in inner magnetospheric dynamics. We challenge the use of the Sym-H index to directly infer temporal variations in the ring current intensity and highlight potential issues with using ring current indices to organize storm time behavior (Borovsky & Shprits, 2017; "Exploration of a Composite Index to Describe Magnetospheric Activity: Reduction of the Magnetospheric State Vector to a Single Scalar," 2018). In order to fully understand the drivers of the Sym-H index and the cause of these reported discrepancies, future work will involve a corresponding investigation into the role of the tail current during storm times, as well as focusing on how the Sym-H index may be corrected to account for nonring current contributions.

Date Availability Statement

All RBSP-ECT data are publicly available at the Web site (http://www.RBSP-ect.lanl.gov/). The solar wind data and Sym-H index data are publicly available online (http://wdc.kugi.kyoto-u.ac.jp/index.html). The SML index and SMU index data are publicly available online (http://supermag.jhuapl.edu). We gratefully acknowledge the SuperMAG collaborators (http://supermag.jhuapl.edu/info/?page=acknowledgement). The GOES magnetometer data are publicly available online (https://www.ngdc.noaa.gov/stp/spaceweather.html). The geomagnetic storm list used in this study is available online (https://doi.org/10.5522/04/11535009.v1).

Acknowledgments
J. K. Sandhu was supported by the NERC Grants NE/P017185/1 and NE/V002554/1. I. J. Rae was supported by the NERC Grants NE/P017185/1 and NE/V002554/1. M.-T. Walach was supported by the NERC Grant NE/P001556/1. Processing and analysis of the HOPE and RBSPICE data were supported by Energetic Particle, Composition, and Thermal Plasma (RBSP-ECT) investigation funded under NASAs Prime contract NAS5-01072.

References

Ahn, B.-H., Chen, G. X., Sun, W., Gjerloev, J. W., Kamide, Y., Sigwarth, J. B., & Frank, L. A. (2005). Equatorward expansion of the westward electrojet during magnetically disturbed periods. *Journal of Geophysical Research*, *110*, A01305. Retrieved from https://doi.org/10.1029/2004JA010553

Antonova, E. (2006). Stability of the magnetospheric plasma pressure distribution and magnetospheric storms. *Advances in Space Research*, *38*(8), 1626–1630.Retrieved from http://www.sciencedirect.com/science/article/pii/S0273117705005661

Antonova, E., & Ganushkina, N. (1997). Azimuthal hot plasma pressure gradients and dawn-dusk electric field formation. *Journal of Atmospheric and Solar-Terrestrial Physics*, *59*(11), 1343–1354.Retrieved from http://www.sciencedirect.com/science/article/pii/S1364682696001691

Antonova, E., Kirpichev, I., & Stepanova, M. (2014). Plasma pressure distribution in the surrounding the earth plasma ring and its role in the magnetospheric dynamics. *Journal of Atmospheric and Solar-Terrestrial Physics*, *115–116*, 32–40.Retrieved from http://www.sciencedirect.com/science/article/pii/S1364682613003179

Belova, E. G., & Maltskv, Y. P. (1994). Supplementary sources of geomagnetic depression during the geomagnetic storm of 8-9 February 1986. *Journal of Atmospheric and Terrestrial Physics*, *56*, 1011–1015. https://doi.org/10.1016/0021-9169(94)90160-0

Borovsky, J. E., & Denton, M. H. (2018). Exploration of a composite index to describe magnetospheric activity: Reduction of the magnetospheric state vector to a single scalar. *Journal of Geophysical Research: Space Physics*, *123*, 7384–7412.Retrieved from https://doi.org/10.1029/2018JA025430

Borovsky, J. E., & Shprits, Y. Y. (2017). Is the dst index sufficient to define all geospace storms? *Journal of Geophysical Research: Space Physics*, *122*, 11543–11547.Retrieved from https://agupubs.onlinelibrary.wiley.com/doi/abs/10.1002/2017JA024679

Burton, R. K., McPherron, R. L., & Russell, C. T. (1975). An empirical relationship between interplanetary conditions and Dst. *Journal of Geophysical Research*, *80*(31), 4204–4214.Retrieved from http://dx.doi.org/10.1029/JA080i031p04204

Buzulukova, N., Fok, M.-C., Pulkkinen, A., Kuznetsova, M., Moore, T. E., Glocer, A., et al. (2010). Dynamics of ring current and electric fields in the inner magnetosphere during disturbed periods: CRCM-BATS-R-US coupled model. *Journal of Geophysical Research*, *115*, A05210. Retrieved from https://doi.org10.1029/2009JA014621

Chapman, S., & Bartels, J. (1940). *Geomagnetism, Vol. II: Analysis of the data, and physical theories*. London: Oxford University Press.
Chapman, S., & Dyson, F. W. (1918). An outline of a theory of magnetic storms. *Proceedings of the Royal Society of London-Series A*, *95*(666), 61–83. https://doi.org/10.1098/rspa.1918.0049
Chapman, S., & Ferraro, V. C. A. (1930). A new theory of magnetic storms. *Nature*, *126*(3169), 129–130.Retrieved from https://doi.org/10.1038/126129a0
Daglis, I. A., Kozyra, J. U., Kamide, Y., Vassiliadis, D., Sharma, A. S., Liemohn, M. W., et al. (2003). Intense space storms: Critical issues and open disputes. *Journal of Geophysical Research*, *108*, 1208. Retrieved from https://doi.org/10.1029/2002JA00972
Daglis, I. A., Thorne, R. M., Baumjohann, W., & Orsini, S. (1999). The terrestrial ring current: Origin, formation, and decay. *Reviews of Geophysics*, *37*(4), 407–438.Retrieved from http://doi.org/10.1029/1999RG900009
Dessler, A. J., & Parker, E. N. (1959). Hydromagnetic theory of geomagnetic storms. *Journal of Geophysical Research*, *64*(12), 2239–2252. Retrieved from http://doi.org/10.1029/JZ064i012p02239
Dubyagin, S., Ganushkina, N., Kubyshkina, M., & Liemohn, M. (2014). Contribution from different current systems to SYM and ASY mid-latitude indices. *Journal of Geophysical Research: Space Physics*, *119*, 7243–7263.Retrieved from https://doi.org/10.1002/2014JA020122
Ebihara, Y., & Ejiri, M. (2000). Simulation study on fundamental properties of the storm-time ring current. *Journal of Geophysical Research*, *105*(A7), 15843–15859.Retrieved from https://doi.org/10.1029/1999JA900493
Ebihara, Y., Ejiri, M., Nilsson, H., Sandahl, I., Milillo, A., Grande, M., et al. (2002). Statistical distribution of the storm-time proton ring current: Polar measurements. *Geophysical Research Letters*, *29*(20), 1969. Retrieved from https://doi.org/10.1029/2002GL015430
Feldstein, Y., Gromova, L., Grafe, A., Meng, C.-I., Kalegaev, V., Alexeev, I., & Sumaruk, Y. (1999). Dynamics of the auroral electrojets and their mapping to the magnetosphere. *Radiation Measurements*, *30*(5), 579–587.Retrieved from http://www.sciencedirect.com/science/article/pii/S135044879900219X
Fok, M.-C., Moore, T. E., & Greenspan, M. E. (1996). Ring current development during storm main phase. *Journal of Geophysical Research*, *101*(A7), 15311–15322.Retrieved from https://agupubs.onlinelibrary.wiley.com/doi/abs/10.1029/96JA01274
Forsyth, C., Rae, I. J., Coxon, J. C., Freeman, M. P., Jackman, C. M., Gjerloev, J., & Fazakerley, A. N. (2015). A new technique for determining Substorm Onsets and Phases from Indices of the Electrojet (SOPHIE). *Journal of Geophysical Research: Space Physics*, *120*, 10592–10606.Retrieved from http://dx.doi.org/10.1002/2015JA021343(2015JA021343)
Friedrich, E., Rostoker, G., Connors, M. G., & McPherron, R. L. (1999). Influence of the substorm current wedge on the Dst index. *Journal of Geophysical Research*, *104*(A3), 4567–4575.Retrieved from https://agupubs.onlinelibrary.wiley.com/doi/abs/10.1029/1998JA900096
Gjerloev, J. W. (2012). The SuperMAG data processing technique. *Journal of Geophysical Research*, *117*, A09213. http://dx.doi.org/10.1029/2012JA017683
Gkioulidou, M., Ukhorskiy, A. Y., Mitchell, D. G., & Lanzerotti, L. J. (2016). Storm time dynamics of ring current protons: Implications for the long-term energy budget in the inner magnetosphere. *Geophysical Research Letters*, *43*, 4736–4744.Retrieved from http://dx.doi.org/10.1002/2016GL068013(2016GL068013)
Gkioulidou, M., Ukhorskiy, A. Y., Mitchell, D. G., Sotirelis, T., Mauk, B. H., & Lanzerotti, L. J. (2014). The role of small-scale ion injections in the buildup of earth's ring current pressure: Van Allen probes observations of the 17 March 2013 storm. *Journal of Geophysical Research: Space Physics*, *119*, 7327–7342.Retrieved from https://agupubs.onlinelibrary.wiley.com/doi/abs/10.1002/2014JA020096
Gonzalez, W. D., Joselyn, J. A., Kamide, Y., Kroehl, H. W., Rostoker, G., Tsurutani, B. T., & Vasyliunas, V. M. (1994). What is a geomagnetic storm? *Journal of Geophysical Research*, *99*(A4), 5771–5792.Retrieved from https://agupubs.onlinelibrary.wiley.com/doi/abs/10.1029/93JA02867
Graham, G. (1724). IV. An account of observations made of the variation of the horizontal needle at London, in the latter part of the year 1772, and beginning of 1723. *Philosophical Transactions of the Royal Society of London*, *33*(383), 96–107. https://doi.org/10.1098/rstl.1724.0020
Greenspan, M. E., & Hamilton, D. C. (2000). A test of the Dessler-Parker-Sckopke relation during magnetic storms. *Journal of Geophysical Research*, *105*(A3), 5419–5430.Retrieved from https://agupubs.onlinelibrary.wiley.com/doi/abs/10.1029/1999JA000284
Hamilton, D. C., Gloeckler, G., Ipavich, F. M., Wilken, B., & Stuedemann, W. (1988). Ring current development during the great geomagnetic storm of February 1986. *Journal of Geophysical Research*, *93*(A12), 14343–14355. https://doi.org/10.1029/JA093iA12p14343
Hutchinson, J. A., Wright, D. M., & Milan, S. E. (2011). Geomagnetic storms over the last solar cycle: A superposed epoch analysis. *Journal of Geophysical Research*, *116*, A09211. Retrieved from https://agupubs.onlinelibrary.wiley.com/doi/abs/10.1029/2011JA016463
Iyemori, T. (1990). Storm-time magnetospheric currents inferred from mid-latitude geomagnetic field variations. *Journal of Geomagnetism and Geoelectricity*, *42*, 1249–1265.
Iyemori, T., Araki, T., Kamei, T., & Takeda, M. (1992). *Mid-latitude geomagnetic indices asy and sym (provisional)*. Kyoto, Japan: Data anal. Cent. For Geomagn. And space Magn., Faculty of Sci., Kyoto Univ.
Iyemori, T., & Rao, D. R. K. (1996). Decay of the dst field of geomagnetic disturbance after substorm onset and its implication to storm-substorm relation. *Annales Geophysicae*, *14*(6), 608–618.Retrieved from https://doi.org/10.1007/s00585-996-0608-3
Jordanova, V. K., Boonsiriseth, A., Thorne, R. M., & Dotan, Y. (2003). Ring current asymmetry from global simulations using a high-resolution electric field model. *Journal of Geophysical Research*, *108*(A12), 1443. Retrieved from https://agupubs.onlinelibrary.wiley.com/doi/abs/10.1029/2003JA009993
Jorgensen, A. M., Henderson, M. G., Roelof, E. C., Reeves, G. D., & Spence, H. E. (2001). Charge exchange contribution to the decay of the ring current, measured by energetic neutral atoms (ENAS). *Journal of Geophysical Research*, *106*(A2), 1931–1937.Retrieved from https://agupubs.onlinelibrary.wiley.com/doi/abs/10.1029/2000JA000124
Kalegaev, V. V., Ganushkina, N. Y., Pulkkinen, T. I., Kubyshkina, M. V., Singer, H. J., & Russell, C. T. (2005). Relation between the ring current and the tail current during magnetic storms. *Annales Geophysicae*, *23*(2), 523–533.Retrieved from https://www.ann-geophys.net/23/523/2005/
Katus, R. M., Liemohn, M. W., Gallagher, D. L., Ridley, A., & Zou, S. (2013). Evidence for potential and inductive convection during intense geomagnetic events using normalized superposed epoch analysis. *Journal of Geophysical Research: Space Physics*, *118*, 181–191. Retrieved from https://agupubs.onlinelibrary.wiley.com/doi/abs/10.1029/2012JA017915
Keika, K., Kasahara, S., Yokota, S., Hoshino, M., Seki, K., Nos, M., et al. (2018). Ion energies dominating energy density in the inner magnetosphere: Spatial distributions and composition, observed by Arase/MEP-i. *Geophysical Research Letters*, *45*, 12153–12162.Retrieved from https://agupubs.onlinelibrary.wiley.com/doi/abs/10.1029/2018GL080047
Kistler, L. M., Mouikis, C. G., Spence, H. E., Menz, A. M., Skoug, R. M., Funsten, H. O., et al. (2016). The source of O+ in the storm time ring current. *Journal of Geophysical Research: Space Physics*, *121*, 5333–5349.Retrieved from https://agupubs.onlinelibrary.wiley.com/doi/abs/10.1002/2015JA022204

Kletzing, C. A., Kurth, W. S., Acuna, M., MacDowall, R. J., Torbert, R. B., Averkamp, T., et al. (2013). The Electric and Magnetic Field Instrument Suite and Integrated Science (EMFISIS) on RBSP. *Space Science Reviews*, *179*(1), 127–181.Retrieved from https://doi.org/10.1007/s11214-013-9993-6

Kozyra, J. U., & Liemohn, M. W. (2003). Ring current energy input and decay. *Space Science Reviews*, *109*(1), 105–131.Retrieved from https://doi.org/10.1023/B:SPAC.0000007516.10433.ad

Krimigis, S. M., Gloeckler, G., McEntire, R. W., Potemra, T. A., Scarf, F. L., & Shelley, E. G. (1985). Magnetic storm of September 4, 1984: A synthesis of ring current spectra and energy densities measured with AMPTE/CCE. *Geophysical Research Letters*, *12*(5), 329–332. Retrieved from http://dx.doi.org/10.1029/GL012i005p00329

Langel, R. A., & Estes, R. H. (1985). Large-scale, near-field magnetic fields from external sources and the corresponding induced internal field. *Journal of Geophysical Research*, *90*(B3), 2487–2494.Retrieved from https://agupubs.onlinelibrary.wiley.com/doi/abs/10.1029/JB090iB03p02487

Le, G., Russell, C. T., & Takahashi, K. (2004). Morphology of the ring current derived from magnetic field observations. *Annales Geophysicae*, *22*(4), 1267–1295.Retrieved from https://www.ann-geophys.net/22/1267/2004/

Li, H., Wang, C., & Kan, J. R. (2011). Contribution of the partial ring current to the SYMH index during magnetic storms. *Journal of Geophysical Research*, *116*, A11222. Retrieved from https://agupubs.onlinelibrary.wiley.com/doi/abs/10.1029/2011JA016886

Liemohn, M. W. (2003). Yet another caveat to using the Dessler-Parker-Sckopke relation. *Journal of Geophysical Research*, *108*(A6), 1251. Retrieved from https://agupubs.onlinelibrary.wiley.com/doi/abs/10.1029/2003JA009839

Liemohn, M. W., Katus, R. M., & Ilie, R. (2015). Statistical analysis of storm-time near-earth current systems. *Annales Geophysicae*, *33*(8), 965–982.Retrieved from https://www.ann-geophys.net/33/965/2015/

Liemohn, M. W., Kozyra, J. U., Thomsen, M. F., Roeder, J. L., Lu, G., Borovsky, J. E., & Cayton, T. E. (2001). Dominant role of the asymmetric ring current in producing the stormtime Dst. *Journal of Geophysical Research*, *106*(A6), 10883–10904. https://doi.org/10.1029/2000JA000326

Lui, A. T. Y. (2003). Inner magnetospheric plasma pressure distribution and its local time asymmetry. *Geophysical Research Letters*, *30*(16), 1846. Retrieved from https://agupubs.onlinelibrary.wiley.com/doi/abs/10.1029/2003GL017596

Mauk, B. H., Fox, N. J., Kanekal, S. G., Kessel, R. L., Sibeck, D. G., & Ukhorskiy, A. (2013). Science objectives and rationale for the radiation belt storm probes mission. *Space Science Reviews*, *179*(1), 3–27.Retrieved from https://doi.org/10.1007/s11214-012-9908-y

Milillo, A., Orsini, S., Delcourt, D. C., Mura, A., Massetti, S., De Angelis, E., & Ebihara, Y. (2003). Empirical model of proton fluxes in the equatorial inner magnetosphere: 2. Properties and applications. *Journal of Geophysical Research*, *108*(A5), 1165. Retrieved from https://agupubs.onlinelibrary.wiley.com/doi/abs/10.1029/2002JA009581

Mitchell, D. G., Lanzerotti, L. J., Kim, C. K., Stokes, M., Ho, G., Cooper, S., et al. (2013). Radiation Belt Storm Probes Ion Composition Experiment (RBSPICE). *Space Science Reviews*, *179*(1), 263–308.Retrieved from https://doi.org/10.1007/s11214-013-9965-x

Mouikis, C. G., Bingham, S. T., Kistler, L. M., Farrugia, C. J., Spence, H. E., Reeves, G. D., et al. (2019). The storm-time ring current response to ICMEs and CIRs using Van Allen Probe observations. *Journal of Geophysical Research: Space Physics*, *124*, 9017–9039.Retrieved from https://agupubs.onlinelibrary.wiley.com/doi/abs/10.1029/2019JA026695

Munsami, V. (2000). Determination of the effects of substorms on the storm-time ring current using neural networks. *Journal of Geophysical Research*, *105*(A12), 27833–27840.Retrieved from https://agupubs.onlinelibrary.wiley.com/doi/abs/10.1029/2000JA000041

Newell, P. T., & Gjerloev, J. W. (2011). Evaluation of SuperMAG auroral electrojet indices as indicators of substorms and auroral power. *Journal of Geophysical Research*, *116*, A12211. http://dx.doi.org/10.1029/2011JA016779(A12211)

Newell, P. T., & Gjerloev, J. W. (2012). SuperMAG-based partial ring current indices. *Journal of Geophysical Research*, *117*, A05215. Retrieved from https://agupubs.onlinelibrary.wiley.com/doi/abs/10.1029/2012JA017586

O'Brien, T. P., & McPherron, R. L. (2000). An empirical phase space analysis of ring current dynamics: Solar wind control of injection and decay. *Journal of Geophysical Research*, *105*(A4), 7707–7719. https://doi.org/10.1029/1998JA000437

Ohtani, S., Nosé, M., Rostoker, G., Singer, H., Lui, A. T. Y., & Nakamura, M. (2001). Storm-substorm relationship: Contribution of the tail current to dst. *Journal of Geophysical Research*, *106*(A10), 21199–21209.Retrieved from http://dx.doi.org/10.1029/2000JA000400

Ozeke, L. G., & Mann, I. R. (2001). Modeling the properties of high-m Alfvén waves driven by the drift-bounce resonance mechanism. *Journal of Geophysical Research*, *106*(A8), 15583–15597.Retrieved from http://dx.doi.org/10.1029/2000JA000393

Perez, J. D., Grimes, E. W., Goldstein, J., McComas, D. J., Valek, P., & Billor, N. (2012). Evolution of CIR storm on 22 July 2009. *Journal of Geophysical Research*, *117*, A09221. Retrieved from https://agupubs.onlinelibrary.wiley.com/doi/abs/10.1029/2012JA017572

Rae, I. J., Murphy, K. R., Watt, C. E., Sandhu, J. K., Georgiou, M., Degeling, A. W., et al. (2019). How do ultra-low frequency waves access the inner magnetosphere during geomagnetic storms? *Geophysical Research Letters*, *46*, 10699–10709.Retrieved from https://agupubs.onlinelibrary.wiley.com/doi/abs/10.1029/2019GL082395

Reeves, G. D., & Henderson, M. G. (2001). The storm-substorm relationship: Ion injections in geosynchronous measurements and composite energetic neutral atom images. *Journal of Geophysical Research*, *106*(A4), 5833–5844. https://doi.org/10.1029/2000JA003017

Roeder, J., Fennell, J., Chen, M., Schulz, M., Grande, M., & Livi, S. (1996). CRRES observations of the composition of the ring-current ion populations. *Advances in Space Research*, *17*(10), 17–24.Retrieved from http://www.sciencedirect.com/science/article/pii/027311779500689C

Rostoker, G. (1972). Geomagnetic indices. *Reviews of Geophysics*, *10*(4), 935–950.Retrieved from https://agupubs.onlinelibrary.wiley.com/doi/abs/10.1029/RG010i004p00935

Sandhu, J. K., Rae, I., Freeman, M., Gkioulidou, M., Forsyth, C., Reeves, G., et al. (2019). Substorm-ring current coupling: A comparison of isolated and compound substorms. *Journal of Geophysical Research: Space Physics*, *124*, 6776–6791.Retrieved from https://agupubs.onlinelibrary.wiley.com/doi/abs/10.1029/2019JA026766

Sandhu, J. K., Rae, I. J., Freeman, M. P., Forsyth, C., Gkioulidou, M., Reeves, G. D., et al. (2018). Energization of the ring current by substorms. *Journal of Geophysical Research: Space Physics*, *123*, 8131–8148.Retrieved from https://agupubs.onlinelibrary.wiley.com/doi/abs/10.1029/2018JA025766

Sandhu, J. K., Yeoman, T. K., & Rae, I. J. (2018). Variations of field line eigenfrequencies with ring current intensity. *Journal of Geophysical Research: Space Physics*, *123*, 9325–9339.Retrieved from https://agupubs.onlinelibrary.wiley.com/doi/abs/10.1029/2018JA025751

Sckopke, N. (1966). A general relation between the energy of trapped particles and the disturbance field near the earth. *Journal of Geophysical Research*, *71*(13), 3125–3130.Retrieved from http://dx.doi.org/10.1029/JZ071i013p03125

Singer, S. F. (1957). A new model of magnetic storms and aurorae. *Eos, Transactions American Geophysical Union*, *38*(2), 175–190. https://doi.org/10.1029/TR038i002p00175

Siscoe, G. L., & Petschek, H. E. (1997). On storm weakening during substorm expansion phase. *Annales Geophysicae*, *15*(2), 211–216. Retrieved from https://doi.org/10.1007/s00585-997-0211-2

Spence, H. E., Reeves, G. D., Baker, D. N., Blake, J. B., Bolton, M., Bourdarie, S., et al. (2013). Science goals and overview of the Radiation Belt Storm Probes (RBSP) Energetic Particle, Composition, and Thermal Plasma (ECT) suite on NASA's Van Allen Probes Mission. *Space Science Reviews*, *179*(1), 311–336.Retrieved from https://doi.org/10.1007/s11214-013-0007-5

Staples, F. A., Rae, I. J., Forsyth, C., Smith, A. R. A., Murphy, K. R., Raymer, K. M., et al. (2020). Do statistical models capture the dynamics of the magnetopause during sudden magnetospheric compressions? *Journal of Geophysical Research: Space Physics*, *125*, e2019JA027289. Retrieved from https://agupubs.onlinelibrary.wiley.com/doi/abs/10.1029/2019JA027289

Stepanova, M., Antonova, E., Moya, P., Pinto, V., & Valdivia, J. (2019). Multisatellite analysis of plasma pressure in the inner magnetosphere during the 1 June 2013 geomagnetic storm. *Journal of Geophysical Research: Space Physics*, *124*, 1187–1202.Retrieved from https://agupubs.onlinelibrary.wiley.com/doi/abs/10.1029/2018JA025965

Sugiura, M., & Poros, D. J. (1964). Hourly values of equatorial Dst for the IGY. *Annals of the International Geophysical Year*, *35*, 9–45.

Takahashi, S., Iyemori, T., & Takeda, M. (1990). A simulation of the storm-time ring current. *Planetary and Space Science*, *38*(9), 1133–1141.Retrieved from http://www.sciencedirect.com/science/article/pii/003206339090021H

Turner, N. E., Baker, D. N., Pulkkinen, T. I., & McPherron, R. L. (2000). Evaluation of the tail current contribution to Dst. *Journal of Geophysical Research*, *105*(A3), 5431–5439.Retrieved from http://dx.doi.org/10.1029/1999JA000248

Turner, N. E., Baker, D. N., Pulkkinen, T. I., Roeder, J. L., Fennell, J. F., & Jordanova, V. K. (2001). Energy content in the storm time ring current. *Journal of Geophysical Research*, *106*(A9), 19149–19156.Retrieved from https://agupubs.onlinelibrary.wiley.com/doi/abs/10.1029/2000JA003025

Usanova, M. E., & Mann, I. R. (2016). Understanding the role of EMIC waves in radiation belt and ring current dynamics: Recent advances. In G. Balasis, I. A. Daglis, & I. R. Mann (Eds.), *Waves, particles, and storms in geospace* (Chap. 10). Oxford: Oxford University Press.

Walach, M.-T., & Grocott, A. (2019). SuperDARN observations during geomagnetic storms, geomagnetically active times, and enhanced solar wind driving. *Journal of Geophysical Research: Space Physics*, *124*, 5828–5847.Retrieved from https://agupubs.onlinelibrary.wiley.com/doi/abs/10.1029/2019JA026816

Welling, D. T., André, M., Dandouras, I., Delcourt, D., Fazakerley, A., Fontaine, D., et al. (2015). The Earth: Plasma sources, losses, and transport processes. *Space Science Reviews*, *192*(1), 145–208.Retrieved from https://doi.org/10.1007/s11214-015-0187-2

Yue, C., Bortnik, J., Li, W., Ma, Q., Gkioulidou, M., Reeves, G. D., et al. (2018). The composition of plasma inside geostationary orbit based on Van Allen Probes observations. *Journal of Geophysical Research: Space Physics*, *123*, 6478–6493.Retrieved from https://agupubs.onlinelibrary.wiley.com/doi/abs/10.1029/2018JA025344

Yue, C., Jun, C.-W., Bortnik, J., An, X., Ma, Q., Reeves, G. D., et al. (2019). The relationship between EMIC wave properties and proton distributions based on Van Allen Probes observations. *Geophysical Research Letters*, *46*, 4070–4078.Retrieved from https://agupubs.onlinelibrary.wiley.com/doi/abs/10.1029/2019GL082633

Zhao, H., Li, X., Baker, D. N., Claudepierre, S. G., Fennell, J. F., Blake, J. B., et al. (2016). Ring current electron dynamics during geomagnetic storms based on the Van Allen Probes measurements. *Journal of Geophysical Research: Space Physics*, *121*, 3333–3346.Retrieved from https://agupubs.onlinelibrary.wiley.com/doi/abs/10.1002/2016JA022358

Zhao, H., Li, X., Baker, D. N., Fennell, J. F., Blake, J. B., Larsen, B. A., et al. (2015). The evolution of ring current ion energy density and energy content during geomagnetic storms based on Van Allen Probes measurements. *Journal of Geophysical Research: Space Physics*, *120*, 7493–7511.Retrieved from http://dx.doi.org/10.1002/2015JA021533